# Chapter 21
# Terahertz Plasmonic Structures

**Adam J. Baragwanath, Andrew J. Gallant and J. Martyn Chamberlain**

**Abstract** Here, we review the background physics of surface plasmons and plasmonic devices. In doing so, we describe how terahertz radiation can be used to excite plasmonic effects. These effects are shown to be beneficial for applications such as terahertz waveguiding, sensing, imaging and wavefront engineering.

## 21.1 Introduction

This chapter deals with terahertz (THz) frequency electromagnetic excitations at the interface between two materials: one is an electrical conductor and the other is a dielectric. The interfaces may be smooth or patterned with pits, corrugations or holes. Key questions, helping us to understand the nature of the excitation or excitations (and their potential application) will include: is a wave or a (quasi) particle perspective preferable; does the excitation propagate, or is it confined to the surface; and how may such a confinement (if it is present) be engineered through the choice of materials or through geometry choice?

This topic has generated considerable interest in the last decade. Applications at THz frequencies are now emerging in the development of: sensors (including biological sensors); techniques for guiding, concentrating and manipulating THz

A. J. Baragwanath
Department of Physics, Durham University, South Road, DurhamDH1 3LE, UK
e-mail: a.j.baragwanath@durham.ac.uk

A. J. Gallant (✉)
School of Engineering and Computing Sciences, Durham University, South Road,
DurhamDH1 3LE, UK
e-mail: a.j.gallant@durham.ac.uk

J. M. Chamberlain
Department of Physics, Durham University, South Road, DurhamDH1 3LE, UK
e-mail: martyn.chamberlain@durham.ac.uk

radiation; and new methods for THz imaging and microscopy. Devices can be constructed using the standard techniques of semiconductor processing technology, as the characteristic length scales are commensurate with the THz wavelength (i.e. a fraction of a millimetre); and so this task can be easily accomplished. The field is often described as plasmonics, by analogy with electronics, to describe the study of the underlying physics and the applications of surface electromagnetic excitations at interfaces. Here, the quasi-particle nature of the excitation is emphasised although it should not be thought that all phenomena are most easily discussed in this way.

A plasmon may be very broadly defined as "a quantum quasi-particle representing the elementary excitations, or modes, of the charge density oscillations in a plasma" [1]. Historically, the topic became of interest to THz specialists in the late 1950s, with observations of the THz frequency emission from ionic plasma in attempted nuclear fusion experiments [2]. Developments in semiconductor material quality and in THz instrumentation led to the first exploration of the properties of the volume (or: bulk, 3D) solid-state plasmon, of which there is an extensive literature [3, 4]. Although this chapter focuses on effects that occur, by definition, at the interface of two materials, it is helpful first to remind the reader of the Drude model of a 3D metal, as it predicts important properties of the material permittivity (or dielectric function), $\epsilon(\omega)$. This model considers a gas of electrons uniformly distributed through a periodic structure of fixed ions and leads to the expression for $\epsilon(\omega)$ at an angular frequency, $\omega$:

$$\epsilon(\omega) = \epsilon_\infty \left[ 1 - \frac{\omega_p^2}{\omega^2 + j\Gamma\omega} \right]. \tag{21.1}$$

In this expression, $\Gamma$ represents a collision rate for electrons and is set at zero for the perfect electronic conductor, or PEC. The (3D) plasma frequency takes on the form: $\omega_p = \sqrt{ne^2/m\epsilon_\infty\epsilon}$, where the (3D) density of electrons is $n$ and all other symbols have their usual meanings. This is the frequency at which the (3D) electron gas oscillates: it lies in the ultraviolet region for metals and in the THz region for semiconductors. The 3D plasmon is the virtual particle of this excitation. From [1], $\epsilon(\omega)$ is complex and so:

$$\Re\left[\epsilon(\omega)\right] = \epsilon_\infty \left[ 1 - \frac{\omega_p^2}{\omega^2 + \Gamma^2} \right]. \tag{21.2}$$

This means that, for a metal, $\Re\left[\epsilon(\omega)\right] < 0$ at $\omega < \omega_p$. When $\omega$ exceeds $\omega_p$, $\Re\left[\epsilon(\omega)\right]$ becomes positive and the material then exhibits dielectric behaviour. In simple physical terms, the electron gas cannot keep pace with the rapidly changing applied electric field. This variation of $\epsilon$ with $\omega$ should be borne in mind when considering the effects at the interface of a metal and a dielectric.

The plasmonic phenomena discussed here may be described by an electromagnetic wave formalism [1]; or, alternatively, a quasi-particle approach can be adopted using the analogy that "the plasmon is to the plasma charge density what the photon is to the electromagnetic field" [5]. In the first approach, all that is needed

is knowledge of how $\epsilon$ varies with frequency and geometry. However, no specific knowledge is required of the actual microscopic processes responsible for the variation of $\epsilon$ for systems such as metal/dielectric interfaces or metal sheets periodically punctured with holes. The quasi-particle view requires an understanding of such processes, including charge movements, scattering and tunnelling, leading to such graphic phrases as "the plasmon rolling like a ball over the landscape" [6]. The reader is warned that a plethora of terms exists in the literature, including: surface plasmon, surface plasmon polariton (SPP), surface electromagnetic excitation (or wave), Zenneck wave, Zenneck–Sommerfeld wave, localised surface plasmons, Brewster modes, local modes, shape modes. . . etc. Furthermore (and to complicate even further), some of these terms may be preceded by adjectives such as: resonant, non-resonant, radiative or non-radiative!

It will be seen in Sect. 21.2 that a very important tool for clarifying and categorising plasmonic phenomena is the dispersion relation, which is a graphical method of relating the wave vector of the entity under discussion to the frequency; or, alternatively, it is the link between its spatial and temporal characteristics. There are many excellent reviews of the general field (including THz applications); and the reader is referred to the classic texts by [1, 7, 8] for a closer discussion. Most of the literature adopts an optical, rather than an electrical engineering, approach to surface plasmons: the concepts of equivalent circuits, characteristic impedances etc. are rarely deployed, although one author [9] has argued that the circuit paradigm provides a clearer basis for discussion.

Plasmonics has advanced significantly (in terms of theory and potential application) due to the discovery of two main phenomena. These are: (a) the so-called Spoof Plasmon effect [6], occurring at THz frequencies at the interface between suitably structured metallic surfaces and a dielectric; and (b) extraordinary optical transmission (EOT) [10], first noted at THz frequencies by Gómez Rivas [11]. The concept of the Spoof Plasmon is discussed later (Sect. 21.2.1), where it is shown that the plasma frequency of a metal can be lowered through the use of surface "decoration." EOT involves a greater-than-expected transmission through an aperture in a metallic substrate. The mechanism of EOT is subject to considerable debate; the reader is referred to reviews by Garcia-Vidal [12] and de Abajo [13] that deal more specifically with the question of radiation passing through periodic arrays of small holes.

The theory of optical transmission through subwavelength holes [14] is considered elsewhere in this Volume. For a subwavelength aperture in an infinitely thin, perfectly conducting substrate, Bethe showed that the transmission efficiency was proportional to $(r/\lambda)^4$, where $r$ is the radius of the aperture and $\lambda$ the incident wavelength. A more comprehensive analysis for real materials, and for substrates of finite thickness, involves tunnelling effects through the aperture and coupling to surface plasmons. This area of investigation has encompassed: single apertures; the 1D case of subwavelength slits; 2D arrays of subwavelength holes of various shapes; together with single apertures flanked by periodic corrugations (bullseye structures). The transmission properties of such systems are governed, *inter alia*, by: hole dimensions, hole shape, array periodicity, ratio of basis-to-lattice, material of array, material

of supporting substrate, angle of incident radiation, frequency of incident radiation and array thickness. Unsurprisingly, there is a vast literature on the topic, including THz observations, theory and applications.

In this context, the observations of R. W. Wood ("Woods anomalies") relating to the dark bands in the reflection spectrum of a metallic grating are of interest. In 1973, the first connection between the presence of Wood's anomalies and the excitation of surface plasmons was introduced. Hutley and Bird [15] drew upon the similarities between experiments conducted by Teng and Stern [16], who used 10 keV electron beams to excite surface plasmons on metal gratings, and Wood's experiments.

This chapter is organised as follows: Sect. 21.2 deals with the background physics of a number of basic plasmonic phenomena; and Sect. 21.3 describes a number of applications of these basic ideas. Finally, there is a short Conclusion. It should be noted that this chapter relates closely to Chap. 15 (Near-field terahertz imaging) and Chap. 22 (Metamaterials). With regard to metamaterials, we adopt the definition that they may be described by a set of effective homogeneous parameters; and that these parameters are determined by the collective response of small conducting resonators [17]. As such, the resonator scale is firmly set in the subwavelength limit. At the microscopic level, however, many of the important aspects of metamaterial performance can be ascribed to plasmonic effects. For further discussion on this matter, the interested reader is referred to articles by: Hibbins [18, 19]; Acuna [20]; and Navarro-Cia [21].

## 21.2 The Physics of THz Plasmonic Phenomena

### 21.2.1 Introductory Theory and Classification of Plasmonic Phenomena

We first present background theory that is relevant to an understanding of plasmonic phenomena at THz frequencies. We review the case of a 2D arrangement, where two semi-infinite half-spaces of different materials (a dielectric and a metal) are juxtaposed. This will enable us to classify plasmonic phenomena and will form the basis of the subsequent analysis of more complicated geometries. It is shown in Sect. 21.2.2 that—by suitable choice of materials—THz frequency surface excitations may propagate at such a simple interface along distances of up to several metres; similarly, the associated electric fields in the dielectric may extend to several millimetres. In Sect. 21.2.3, we consider how this situation is altered if the surface is "decorated" with simple corrugations. This theme is continued in Sect. 21.2.4: we shall see how significant confinement effects can be engineered through choice of surface geometry. The remainder of the section deals with THz frequency properties of arrays of holes and gratings formed on metallic surfaces.

A rigorous analysis of the electromagnetic modes supported in a materials arrangement, depicted in Fig. 21.1, is given from a systems perspective in [1]. As noted pre-
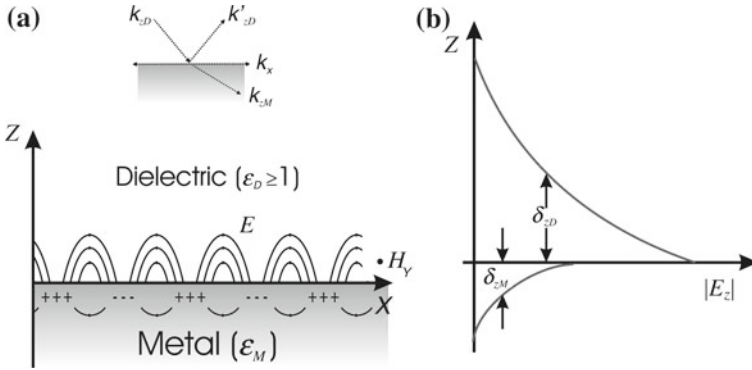
**Fig. 21.1** **a** Representation of an SPP at the boundary between a metal and a dielectric. Subscripts (*M, D*) represent metal and dielectric, respectively; the superscript (') indicates a reflected wavevector. **b** The relative decay of the electric field into the dielectric and the metal (*top* and *bottom* respectively)

viously, in this approach all that is necessary is to know the geometry and the value of $\epsilon(\omega)$. More physical insight may be gained from simple treatments [7, 8, 22] which consider a wave incident on the interface through the dielectric at some angle $\theta_i$ to the normal; and with electric vector in the plane of the paper. The case of most interest is when $\theta_c = \sin^{-1}\left[\sqrt{\epsilon_M}/\sqrt{\epsilon_D}\right]$. Above this critical angle, radiation does not propagate in the metal: the oscillating electric field is then totally reflected, but interface bound charges will oscillate, giving rise to strongly decaying (evanescent) fields at the interface between the two materials. A more detailed analysis [1] leads to the conclusion that, when $\omega < \omega_p$, the surface wave is trapped with exponential decays of the amplitude of the electric field amplitude into both media provided that $\epsilon_D(\omega)$ is positive and $\epsilon_M(\omega)$ is negative. Further discussion of the extent of this trapping, or confinement, is given later.

By solving Maxwell's equations with the appropriate boundary conditions, the excitation dispersion relation can be determined for the propagation direction ($x$) and for the direction normal to the boundary ($z$), into the dielectric and metal, respectively [7]:

$$k_x = \frac{\omega}{c}\sqrt{\frac{\epsilon_D\epsilon_M}{\epsilon_D + \epsilon_M}} \tag{21.3}$$

and

$$k_{z,D} = \frac{\omega}{c}\sqrt{\frac{\epsilon_D^2}{\epsilon_D + \epsilon_M}}, \tag{21.4a}$$

$$k_{z,M} = \frac{\omega}{c}\sqrt{\frac{\epsilon_M^2}{\epsilon_D + \epsilon_M}}. \tag{21.4b}$$

**Table 21.1** The types of EM modes existing at a planar dielectric/metal interface, assuming $\epsilon_D > 1$. After [1]

| Mode | $\Re(\epsilon_M)$ | $\Im(\epsilon_M)$ | Nature of $k_x$ | Nature of $k'_{zD}$ | | Nature of $k_{zM}$ | |
|---|---|---|---|---|---|---|---|
| | | | | $\Re$ | $\Im$ | $\Re$ | $\Im$ |
| Brewster modes | $>0$ | $=0$ | Real | $>0$ | $=0$ | $>0$ | $=0$ |
| | $>0$ | $>0$ | Complex | $>0$ | $<0$ | $>0$ | $>0$ |
| Localised SPPs | $0 > \Re(\epsilon_M) > -\epsilon_D$ | $=0$ | Pure imaginary | $<0$ | $=0$ | $>0$ | $=0$ |
| | $0 > \Re(\epsilon_M) > -\epsilon_D$ | $>0$ | Complex | $>0$ | $<0$ | $<0$ or $>0$ | $>0$ |
| Propagating SPPs | $\epsilon_D > \Re(\epsilon_M)$ | $=0$ | Real | $=0$ | $<0$ | $=0$ | $>0$ |
| | $\epsilon_D > \Re(\epsilon_M)$ | $>0$ | Complex | $>0$ | $<0$ | $<0$ or $>0$ | $>0$ |

Note that, the excitation is generally described as a SPP, using the quasi-particle nomenclature, and recognising the implicit coupling between photon and plasmon. In the above equations, the subscripts refer to the SPP $k$-vector components (see Fig. 21.1a for clarity) these are allowed to be complex for real $\omega$. For an excitation propagating along the interface, the wave vector $k_x$ remains real. To ensure that the surface excitation remains bound, the normal components of the wave vector $k_z$ must be imaginary so that the field decays evanescently away from the interface. Whether or not these conditions will be met depends critically on the values of the real and imaginary parts of $\epsilon_D$ and $\epsilon_M$, which leads to a helpful way to categorize the modes that can be sustained at the interface.

Table 21.1 summarises all the modes; an analogous diagrammatic treatment is given by [1]. The region in Table 1 corresponding to the *Brewster modes*, exists when $\Re(\epsilon_M) > 0$. For a real metal, i.e. when $\Im(\epsilon_M) > 0$, these modes can be regarded as true surface modes. These surface polaritons comprise a mixture of surface charge waves and propagating photons. Strictly speaking, these entities are not conventionally described as surface *plasmon* polaritons; this classification is reserved for the case when $\Im(\epsilon_M) > 0$. In practice, Brewster modes are not encountered at THz frequencies for metal/dielectric or semiconductor/dielectric interfaces.

The modes corresponding to those labelled *localised* SPPs possess a non-propagating surface wave, highlighted by the pure imaginary value of $k_x$. For a perfectly electrically conducting (PEC) material, i.e. when $\Im(\epsilon_M) = 0$, these modes can be considered radiative as the evanescent energy of the surface wave is dissipated away from the surface via the real, propagating $k_z$ modes. Such modes become non-radiative for the case of a real metal as the $k_z$ modes become evanescent i.e. they can no longer radiate the evanescent surface wave. The role of localised SPPs at THz frequencies will be discussed later, in the context of a patterned conducting surface.

Finally, we consider propagating SPPs, for which $\epsilon_D > \Re(\epsilon_M)$. The pure imaginary nature of both $k_{zD}$ and $k_{zM}$ display the evanescent decay of the field perpendicular to the surface, whilst the real value of $k_x$ highlights the propagating nature of the established surface wave. These non-radiative modes are known formally as propagating SPPs; they are fully trapped at the conductor–dielectric boundary. For a real metal, the imaginary nature of $k_x$ results in these modes becoming pseudo-
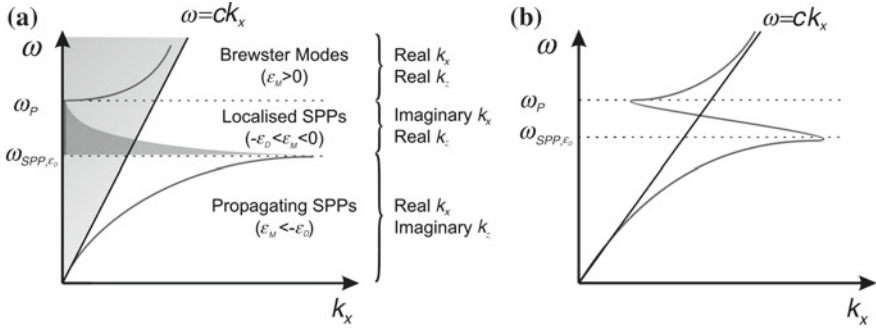
**Fig. 21.2 a** Dispersion relation for a lossless Drude metal. Free-space photons lie in the shaded light grey region, to the left of the *light line*. The broadening of the localised SPPs (indicated by the shaded *dark grey* region) arises due to the strong evanescent nature of these modes. **b** Dispersion relation when losses are included. After [1]

propagating i.e. there is only a certain distance the SPPs can travel before damping-induced losses imposed by the metal become overwhelming.

Figure 21.2 shows two versions the dispersion relation ($\omega$, $k_x$). Other reviews [1, 7, 8] discuss: the derivation of this relation; the importance of the regions of the dispersion relation diagram; and effects of absorption and loss in the metal. We now consider a few salient points, however, for future reference. The first is that the *light line*, which separates allowable free-space photons from the compound excitations. Second, between the Brewster modes and the propagating SPPs reside the localised SPP modes. In this region, a significant broadening of the mode is often observed due to the metallic losses. The propagating SPP branch can be seen to approach the limiting frequency $\omega_{\mathrm{SPP}}$ as $k_x$ increases.

For a perfect Drude metal, this frequency can be shown to be [7]:

$$\omega_{\mathrm{SPP}} = \frac{\omega_p}{\sqrt{(1 + \epsilon_D)}}. \tag{21.5}$$

Sometimes this is referred to as a pure surface plasmon (dropping "polariton") to emphasise the surface-wave-like nature of the excitation. At lower frequencies the propagating SPP mode approaches the light line, where these modes take on a more "photon-like" appearance [1], behaving more as a photon travelling at grazing incidence. Alternatively, the wave-like nature of the entity is highlighted by describing it as a Zenneck Wave [23, 24].

**Fig. 21.3** Variation of $\Re(\epsilon)$ (*solid lines*) and $\Im(\epsilon)$ (*dashed lines*) with frequency for **a** gold and **b** InSb. After [26], ©2009 IEEE
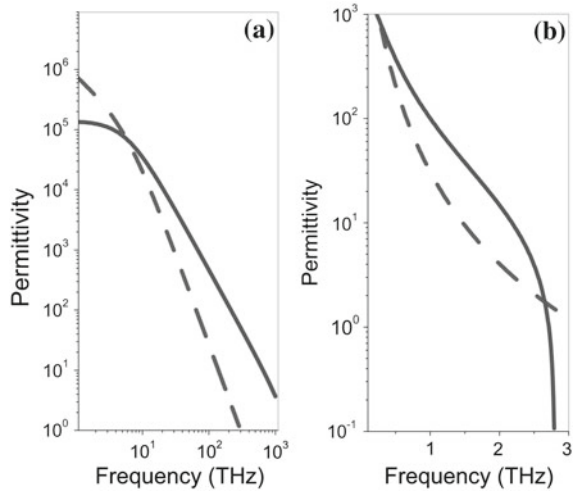


### 21.2.2 THz Frequency Plasmons at the Planar Metal/Dielectric Interface

The extent of localization of the SPP, as measured by the propagation distance along the interface and by the electric field attenuation perpendicular to the interface, are of great importance. The main results are: (a) the SPP wavelength is given by $\lambda_{SPP} = 2\pi/\Re(k_x)$; and (b) the imaginary component of the SPP wave vector component in the $x$ direction provides a measure of the propagation length along the surface $L_{SPP} = 1/2\Im(k_x)$. The decay length of the mode from the interface into either the metal or the dielectric is $L_{z,l} = 1/2\Re(k_{z,l})$, where: $k_{z,l}$ is the complex perpendicular wave vector component; $l$ is an index (1 = dielectric, 2 = metal) and $k_{z,l} = \sqrt{k_x^2 - \epsilon_1(\omega)\left[\frac{\omega}{c}\right]^2}$.

It is instructive to determine these values at a frequency of 1 THz for interfaces between gold and air and between the high mobility semiconductor indium antimonide (InSb) and air. Using the materials data [25] for these two materials, Fig. 21.3 [26] shows the variation of $\Re(\epsilon)$ and $\Im(\epsilon)$ for these two materials. Note that, the frequency scales differ markedly. Using this information, together with the previous equations, values for $\lambda_{SPP}$, $L_{z1}$ and $L_{SPP}$ may be calculated [26]. Table 21.2 shows these values at 1 THz. Clearly, for gold, the much higher electron density ($5.9 \times 10^{28}$ m$^{-3}$) gives rise to a larger value for $\omega_p$ than for InSb (electron density $2 \times 10^{22}$ m$^{-3}$), leading to larger values of the permittivity, $\epsilon$, and hence greater impedance mismatch at the air interface and greater penetration into the air. Furthermore, the excitation propagates several metres along the gold surface as a direct result of the weak wave/surface interaction. Also apparent are: the stronger confinement for InSb; and that, as the frequency approaches $\omega_p$, a less than one-wavelength confinement is possible, breaking the Rayleigh limit.

**Table 21.2** Parameters at 1 THz for interfaces between air and two conducting materials, Gold and InSb. After [26], ©2009 IEEE

| Material | $n(\text{cm}^{-3})$ | $\omega_p/2\pi$ (THz) | $\Re(\epsilon_M)$ | $\Im(\epsilon_M)$ | $\lambda_{\text{SPP}}$ (m) | $L_{\text{SPP}}$ (m) | $L_{z1}$ (m) | $L_{z2}$ (m) |
|---|---|---|---|---|---|---|---|---|
| Gold | $59 \times 10^{27}$ | $2.2 \times 10^3$ | $-86 \times 10^3$ | $0.62 \times 10^6$ | $0.3 \times 10^{-3}$ | 30 | $25 \times 10^{-3}$ | $40 \times 10^{-9}$ |
| InSb | $20 \times 10^{21}$ | 2.8 | $-99$ | 30 | $0.29 \times 10^{-3}$ | $15 \times 10^{-3}$ | $0.24 \times 10^{-3}$ | $2.3 \times 10^{-6}$ |
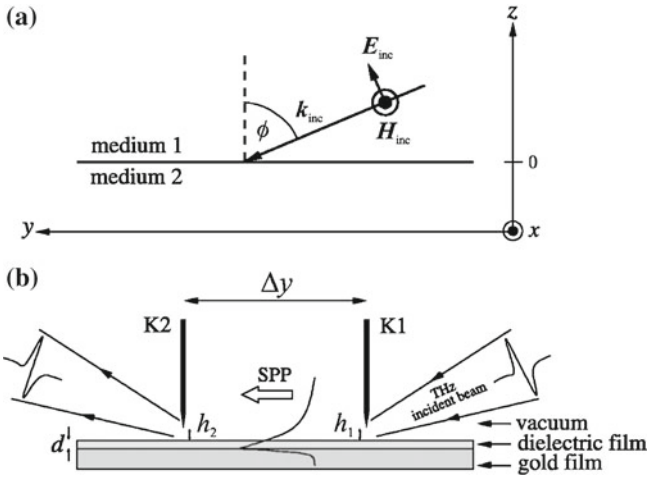
**Fig. 21.4** Aperture excitation geometry. Reprinted figure with permission from [34]. ©2004 by the American Physical Society

From Fig. 21.2, in order to satisfy quasi-momentum conservation, it is necessary to provide an additional wave vector component to the SPP. At visible and near-infrared frequencies prism coupling is normally used [27]. This approach has been described for THz SPP studies using Teflon [28] and silicon [29] prisms to measure, respectively: the THz frequency permittivity of the semiconductor InAs and of distilled water; and the propagation of SPPs along thin plastic films. However, the most-favoured approach at THz frequencies is to use a broadband aperture excitation technique [30] originally developed for second harmonic generation, as shown in Fig. 21.4. The method has been used to investigate the propagation of SPPs along silicon [31] and InSb surfaces [32], in both cases demonstrating that confinement of SPPs takes place on semiconductors at THz frequencies in a similar fashion to metals at shorter wavelengths. Whilst the propagation of SPPs along simple interfaces between air and a metal (or semiconductor) is of some interest, there are important applications of the measurement method in sensing the properties of thin films of biological or plastic materials placed on such interfaces. The problem was first discussed by Kaminow [33] who argued that greater confinement is obtained with shorter wavelengths. Maier [8] analysed a three component system e.g. a metal/plastic film/air layering. Saxler [34], using the aperture excitation technique, investigated SPP phenomena in cyclotene films laid on gold. Saxler probed the spatial and spectroscopic field distribution of the SPPs and concluded that stronger confinement to the surface occurs in the presence of the dielectric film. Related experiments are described by Isaac [35] who claims that the properties of deposited films that are as thin as 50 nm may be probed using this method.

Jeon [36] gives a thorough overview of the THz Zenneck wave, discussing in some detail if this is truly a Zenneck wave (i.e. propagating significant distances in

a loss–less fashion). A waveguide arrangement is deployed to launch the wave over the metal surface and Jeon concludes that deficiencies in the launching system will prevent true Zenneck wave behaviour. This is a very pertinent point, often disregarded by other authors, that all elements in the "circuit" need to be designed together. Gong [37] considers the large evanescent field associated with the very weak guiding of the Zenneck wave over the smooth metal. Gong shows, experimentally, that a very thin dielectric layer will reduce the extent of the field 100-fold, demonstrating the potential of the arrangement for sensing applications.

### 21.2.3 Corrugated Structures with Characteristic Dimensions Commensurate with the THz Wavelength

As a preliminary to the discussion of a spoof plasmon in Sect. 21.2.4, we consider a metal surface decorated with corrugations of dimensions that are commensurate with the THz wavelength. In these arrangements, a hole is frequently used to sample the THz radiation; this section therefore also serves as an introduction to Sect. 21.2.5, where the phenomenon of EOT is considered in more detail. The geometry in which a hole is flanked by annular corrugations is termed a bullseye. However, to begin this discussion we consider first the experiments of Zhu [38] who measures the vector components [39] of the THz electric field at the centre of a bullseye which is not pierced with a central hole (see Fig. 21.5). The bullseye consists of 25 concentric annular grooves each of rectangular cross-section, with a width of 500 µm and a depth of 100 µm; the centre-to-centre spacing is 1 mm. The bullseye is illuminated vertically by a broadband THz beam from a standard time-domain spectroscopy (TDS) system with frequency range approximately 100 GHz to 1.5 THz. The electric field at the centre of the bullseye is measured with an electro-optic detector; and the use of a TDS system enables the temporal build-up of the signal to be monitored. Note that coupling of the THz beam with the structure takes place with normal incidence geometry, in contrast to coupling discussed previously. Caglayan [40] argues that the coupling is effective because the periodic grating structure of the bullseye provides additional pseudo-momentum; however, coupling can also be obtained for normal incidence even when there is only one annular ring present [41]. A pragmatic explanation is to simply state that scattering and diffraction will occur as the THz beam hits the metallic corrugation, coupling to surface plasmons; these will then propagate as SPPs to the next corrugation, where the same process takes place again. The resonant corrugation structure thus encourages the build-up of a signal at a wavelength corresponding to the grating period. This may be easily seen in the time-domain trace (Fig. 21.5) as the detector receives signals carried by successive pulses of SPPs.

Propagation also occurs in the direction from the centre towards the edge of the array; but these SPPs are not captured by the detector. The vector field of the THz wave can be measured and this shows an expected exponential fall-off away from the metal surface. Note that, the SPPs involved here (where the surface features are
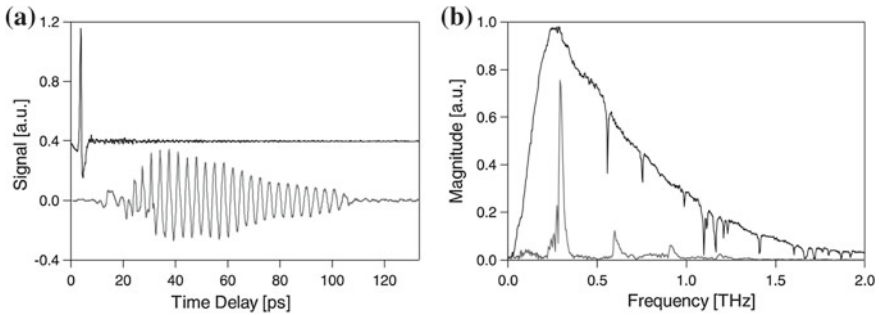
**Fig. 21.5** Measured time-domain waveforms for the incident THz pulse (*upper waveform*) and the $E_z$ component of the THz surface plasmon measured at the centre of the bullseye structure. The waveforms, offset vertically for clarity, were measured under different experimental configurations. Reprinted with permission from [38]

not obviously subwavelength) are the same as those discussed previously; and that the major role of the corrugations is to assist the coupling process, and not to provide confinement *per se*.

Before proceeding to discuss bullseyes with a central hole, it is first helpful to comment on the process of transmission of light through a very small hole that has no intentional surface decoration. This is discussed in detail elsewhere in this Volume for THz frequency radiation: the process involves an evanescent coupling between the plasmons on the input surface, through the orifice, to the output surface where re-radiation occurs. Following transmission measurements through subwavelength (300 nm diameter) holes at optical frequencies ($\lambda \approx 600$ nm), it was found that: unexpected enhancements occurred in the transmission of the hole and the directionality of the emerging beam; and that the hole shape was important in controlling these. Using electron-beam-induced plasmon emission, it was deduced that: localised surface plasmons are excited on the incident face; and that these subsequently tunnel through the hole, before re-radiation at the exit surface. This basic approach is used to account for the THz transmission studies of Agrawal [41, 42] who investigated the transmission properties of bullseye structures with central holes using TDS measurements. The geometry of these structures is very similar to that used by Zhu [38]; bullseyes with one, two, four and six grooves are considered with separation of the order of the incident wavelength. As may be seen [38], the TDS method enables the contributions of the coupling of the incident THz wave to each successive annular groove to be followed directly. Studies of the effect of groove depth and width are reported [41] leading to the possibility of control of the transmitted pulse shape. It is noted, empirically, that a depth of roughly one-tenth of the wavelength provides best coupling. The effects of changing the phase of the annular grooves with respect to the central aperture have also been studied [43]; the transmitted intensity can be manipulated, from enhancement to suppression, as the phase is changed. The inclusion of a defect onto the surface pattern structure (i.e. the absence of a groove) also shows up on the TDS trace as a suppressed oscillation at a specific temporal location [42].

The explanation of all of these phenomena is in terms of coupling of the THz radiation to surface plasmons to form SPPs with a resonant frequency, caused by the array periodicity, followed by tunnelling through the aperture and subsequent re-radiation. There may, in addition, be a non-resonant direct transmission through the aperture.

Finally, note that patterning the exit face of the metal with a similar annular groove pattern [44] adds an additional component to the overall process: the initial coupling of radiation to the input face is followed by the propagation of resonant SPPs towards the aperture and subsequent tunnelling through it. The exit process itself has two components: the first is direct radiation into the far-field of the aperture; the second is from SPPs that propagate along the exit face but, because of the corrugations on that face, will radiate into the forward (exit) direction. If the exit face were plane, then the SPPs would be bound to the interface and subsequently attenuated, so that the integrated intensity of the transmitted radiation would be less i.e. the presence of any exit face corrugations can be said to enhance the output power.

The plasmons considered above are "genuine" plasmons, with properties such as confinement and propagation length primarily determined by the nature of the interface conductor. The corrugations, separated by a distance of the order of the wavelength, mainly act as centres for plasmon/photon scattering and coupling. We now consider the case of distinctly subwavelength features, where the geometry dictates confinement to a much greater extent.

## *21.2.4 The Spoof SPP*

Techniques to improve surface wave confinement have been researched for several decades. For transmission lines, Goubau [45] reported that surface wave confinement could be enhanced by structuring the metal surface of a wire. A series of corrugations at the air/metal interface act to increase the electric field penetration into the interface and therefore reduce the impedance mismatch. In 2004, Pendry [6] addressed specifically the case for confining SPPs at the surface of PECs. This is particularly pertinent to the THz region where, on first inspection, metals appear not to be well suited for SPP confinement. The Drude model shows that the permittivity of a metal tends to that of a perfect electrical conductor (i.e. minus infinity) at frequencies much lower than $\omega_p$. In the THz region, for metals, both the real and imaginary parts of the permittivity are many orders of magnitude greater than those at visible frequencies. This leads to a high impedance mismatch at the metal/dielectric interface, and hence poor confinement of the SPP to the surface.

As discussed in the previous section, for metals at THz frequencies, an SPP is really travelling as a weakly confined, lossy, wave. In order to move from this regime to that of a bound SPP, the metal/dielectric interface must be modified to reduce the impedance mismatch. Pendry considered the problem from an "effective medium" perspective where both the permittivity and permeability of the metal are tailored by machining arrays of sub wavelength indentations or holes. Unlike our discussions in previous sections, the surface decorations for the Pendry case must be subwavelength both with regards to their feature size and their spacing. Hence, the features are not

"seen" individually by the incident radiation; instead, they collectively create an artificial material which has an effective permittivity and permeability.

Importantly, Pendry showed that a structured metal can have an effective plasma frequency which is lower that of a bulk metal. In simple terms, the holes dilute the plasma frequency of a metal. For the square hole array case, where the hole is filled with a material of permittivity $\epsilon_h$ and permeability $\mu_h$, the effective plasma frequency, $\omega'_p = \pi c_0 / a \sqrt{\epsilon_h \mu_h}$ [6, 13]. This corresponds to the cut-off frequency of the hole for $TE_{01}$ when the hole is considered as a waveguide. Hence, the plasma frequency of metal can be lowered through surface decoration into the THz region. This enables a structured metal/dielectric interface excited with THz (and microwave) frequencies to show surface wave confinement comparable to that found at semiconductor/dielectric interfaces (e.g. InSb/air). The conditions are thus met for bound SPPs. Pendry referred to the SPPs generated through the use of structured surfaces as "spoof" SPPs, i.e. imitations of "genuine" plasmons. From a device implementation perspective, the bound spoof SPP concept is very significant. Confined SPP effects can be achieved, in the THz region, at metal/air rather than just semiconductor/air interfaces. A plethora of surface micromachining techniques, usually adapted from the integrated circuit industry, are available for the fabrication of these spoof metal surfaces.

Williams [46] experimentally confirmed the existence of spoof SPPs on a metal in the THz region. They used THz TDS to measure SPP propagation along copper surfaces patterned with arrays of micromachined square pits and showed wavelength scale confinement over an octave of THz frequency. Williams used diffraction at a knife edge to launch the spoof SPPs. It should be appreciated that the quasi-momentum conservation arguments outlined previously as requirements for the coupling of incident radiation to "genuine" SPPs also hold for spoof surfaces. For example, Hibbins [47], reported the use of a wax prism to launch a spoof SPP on a metal at microwave frequencies.

So far, we have considered planar surfaces for the propagation of SPPs. However, similar effects can be observed with cylindrical conductors (i.e. wires). This geometry was first considered by Sommerfeld in 1899 [48]. However, more recently it has proved attractive for the guided propagation of THz pulses. Bare metal wires provide low signal attenuation and dispersion compared to conventional parallel plate waveguides, coax or fibres [49]. Furthermore, several groups have shown that by tapering the end of a wire [50–52], the electric field can be confined into a subwavelength spot. However, along the length of the wire, the radial electric field confinement of the SPPs typically spans several wavelengths. This poor confinement can be exploited as a mechanism to couple between wires (e.g. for a beam splitter) [49]. However, a key disadvantage is that a poorly confined SPP suffers from bending losses [53]. This fundamentally limits the ability to use this type of guided propagation in compact, integrated, THz systems.

As with planar surfaces, spoof SPPs also provide a mechanism for well-confined transmission of terahertz radiation along wires [54]. Figure 21.6 shows a tapered wire configuration decorated with sub wavelength periodic grooves. Simulations with this geometry suggest subwavelength confinement of the electric field along the length of the wire and deep subwavelength confinement at the tip. As will be discussed further

**Fig. 21.6** Superfocusing on a corrugated cone of length 2 mm with constant groove depth of 5 μm and a lattice constant 50 μm. The radius, R, is reduced from 100 to 10 μm, demonstrating how the *E* field can be focussed and concentrated at the tip of conical structures. The plot shows the magnitude of the *E* field on a logarithmic scale spanning 2 orders of magnitude. Reprinted figure with permission from [54]. ©2006 by the American Physical Society
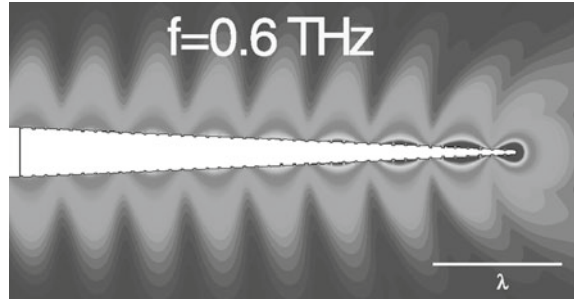


in Sect. 21.3, this has applications in the sensing and imaging of small quantities of material.

Finally, an alternative approach, employed by Chau [55] to lower the plasma frequency of a metal, is to use ensembles of subwavelength sized metallic particles. As with the micromachined devices presented previously, the subwavelength particles collectively have an effective permittivity (and permeability) which differs from that of their bulk. Chau observed THz pulse transmission through metallic particles which were randomly distributed in a sample cell. This transmission was through collective thicknesses ($\approx$1.2 mm), much greater than the skin depth of the metal, and demonstrated a positive permittivity. In this configuration, the SPPs are formed at the surface of the metallic particles; coupling (and, hence, SPP propagation) occurs between the closely spaced particles [55].

## 21.2.5 Gratings and Arrays of Apertures

### 21.2.5.1 Introduction

There is as yet no unequivocal explanation for the phenomenon of EOT through 2D subwavelength hole arrays [10]. Although it is generally acknowledged that SPPs play a vital role in this observed "anomaly," the precise nature of transmission through the array is hotly debated [56–65]; with some authors [66, 67] even claiming no role for SPPs. We present, first, an outline of how the presence of a 2D array affects the dispersion relation of SPPs. An overview will then (Sect. 21.2.5.2) be given of the mechanisms thought to be involved in transmission; and how these are affected by the hole shape and size, the lattice arrangements, material geometry, material properties and thickness.

When light is incident upon a 2D metal hole array with subwavelength holes and periodicity, each hole edge serves as a diffraction point at which *p*-polarised light can couple to SPPs. The 2D lattice provides in-plane momentum with integer multiples of $2\pi/L$ in both the *x* and *y* directions, where *L* is the period of the array. This increased in-plane momentum allows the freely propagating light to couple to SPP modes, which are subsequently initiated along the metal–dielectric boundary. The wave vector of the SPP can thus be expressed as:

$$k_{\text{SPP}} = \frac{2\pi}{\lambda} \sin\theta \pm mG_x \pm nG_y \qquad (21.6)$$

Here, $\lambda$ is the wavelength of the incident radiation, $\theta$ is the angle of incidence of light on the array, *m* and *n* are integers whilst $G_x$ and $G_y$ are the reciprocal lattice vectors in the *x* and *y* directions, respectively. For the case of a square array, $G_x = G_y = 2\pi/L$. After propagating along the metal, the established SPPs are subsequently re-emitted into free-space light upon arrival at another diffraction point. The spatial periodicity of the array results in a periodicity existing for the wave vector of the SPP modes, which allows for Bloch wave and Brillouin zone analogies to be drawn. The folding of the Bloch wave vector at the Brillouin zone boundary results in resonant frequencies at the $\Gamma$ point that are a function of the lattice constant. Ultimately, for normal incidence, the transmission peak resonances are approximated by the following relationship, confirming the strong dependence on the lattice constant [60]:

$$\lambda_{\text{peak}} = \frac{L}{\sqrt{(m^2 + n^2)}} \sqrt{\epsilon_D}. \qquad (21.7)$$

Dispersion curves for SPPs on a 2D hole array display transmitted resonant frequencies as a function of incident angle. The $(m, n)$ nomenclature corresponds to integer steps taken along the reciprocal lattice, and serve as a label for the resonances. Taking such steps in reciprocal space ultimately maps out diffraction spots, allowing an equivalence to be drawn for the observed resonances: the wavelengths responsible for a particular transmission resonance correspond to missing diffraction spots, due to the wave being "trapped" along the surface [68]. The 2D nature of the periodicity results in momentum gained from the *y* component being projected onto the *x* diagram. A typical dispersion curve for a 2D metal hole array for the $\Gamma - x$ orientation can be seen in Fig. 21.7.

The black curves in Fig. 21.7 are similar to those for a periodic array of subwavelength slits and display *p*-polarised characteristics only. The light grey curves correspond to the momentum gained from *y* periodicity, which is projected onto the orientation. These curves display a mixture of *p* and *s* polarisation characteristics, highlighted by their flatter appearance and lack of splitting with increasing angle. At 0° incidence angle, multiple resonance peaks are observed highlighting how transmission can be enhanced over a wide frequency range, even for perpendicular illumination. All the higher order modes lie to the left of the light line; such

**Fig. 21.7** Typical dispersion curve for a 2D metal hole array for orientation. *Black curves* correspond to momentum contributions from *x* periodicity, whilst *light grey curves* display *y* projected momentum. The *dark grey dotted line* corresponds to the standard surface plasmon dispersion curve. After [69]
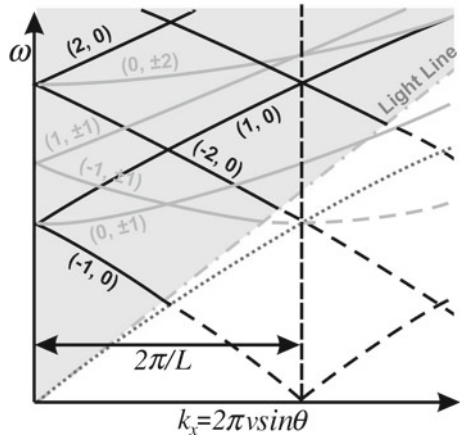


modes can be excited without the need for prism coupling, i.e. they can be excited using free-space light.

Two-dimensional gratings are an extremely elegant tool for both the study and exploitation of SPPs; not only does the physical structure of the array generate SPPs without need for a further coupling mechanism, but the "dilution" of the metal with dielectric filled holes acts to increase the confinement of the SPPs to the metal surface. The following section will review experiments undertaken on 2D hole arrays at THz frequencies, summarising the current proposed theories for EOT and the other associated anomalies.

### 21.2.5.2 Phenomenology and Theory

The first demonstration of enhanced THz transmission through a 2D subwavelength hole array was undertaken by Gómez Rivas [11]. Using a doped silicon substrate (doped so that the plasma frequency was in the THz region), hole arrays were created using perpendicular cuts of a wafer saw on both sides of the silicon wafer. Strong resonant peaks were observed not only at the cut-off frequency for the holes, but more unexpectedly, also at much lower frequencies. The position of the resonant peaks was correlated to the period of the array, whilst thinner substrates were shown to improve dramatically overall transmission.

The work of Qu et al. was the first to display THz EOT through a metallic subwavelength hole array at THz frequencies [70], a regime in which metals should classically be unable to support SPP modes due to their PEC properties. Lithographically patterned aluminium hole arrays on high resistivity silicon substrates displayed SPP resonances for both the metal–silicon and metal–air interfaces, with rectangular holes showing increased transmission and phase shift over circular counterparts. Much sharper resonances were observed for the case of free-standing metal

foil hole arrays [71], owing to the increased coupling between SPPs on the front and back of the array, as previously observed in the optical regime [61]. Resonances continued to 100 ps (in the time domain), displaying a long SPP lifetime and ultimately a long propagation distance. This work was also the first to test different metals for the same array and hole dimensions by sputtering optically thick silver on the original aluminium foil. Resonances were found to appear at the same frequencies for each metal; but a change in the magnitude of the transmitted resonance was observed. This has been confirmed in further work, where even poor conductors such as lead were found to support SPPs, with the transmitted intensity dominated by the ratio of the real to imaginary parts of the metal dielectric constant [72]. Interestingly, SPP resonances have also been found to exist on metals whose thickness is less than the skin depth, with the strength of the resonance increasing with increasing thickness [73]. THz transmission through superconducting plasmonic hole arrays has also been reported [74].

Much work has been undertaken to optimise conditions for SPPs in 2D hole arrays at THz frequencies. Janke et al. were the first to analyse the effect of varying hole shape, where square holes of varying sizes were made in a doped silicon array [75]. Increased transmission was observed for holes of increasing size; however the resonances became broader, indicating a decreased surface lifetime for the SPPs with increasing hole width. The resonances observed in this experiment differed from the predictions calculated using Eq. 21.7 due to the presence of channelled grooves on the substrate (as a consequence of the fabrication process). The presence of these grooves will dramatically alter the coupling and decoupling of SPPs and subsequent transmission through the holes. The importance of hole orientation has also been demonstrated [76] using elliptical hole arrays in ultra-thin, doped silicon wafers. When the long axis of the ellipses were aligned perpendicular to the polarisation of the $E$-field, vast transmission was observed for frequencies well below that of the cut-off. Rotating the sample through $90°$ shifted the position of the resonance to higher frequencies, and drastically reducing the transmission. The strong transmission for the initial orientation was attributed to the greater preservation of beam polarisation over the second direction, as confirmed in [70].

Further detailed studies investigating how the hole shape affects the transmission have been carried out using free-standing metal foils [71]. Greater transmission was found to occur for non-symmetric holes compared with the symmetric case. This work also displayed that as the aspect ratio of a rectangular hole (aligned with the long axis perpendicular to the polarisation of the $E$-field) was increased, the relative transmission decreased. Furthermore, results found in the optical regime, where a decreasing aperture width redshifts the resonant frequency [77, 78], were not replicated here; the frequency remaining almost constant. Importantly, this work was the first to recognise the onset of the SPP resonance occurring after that of the direct (non-resonant) transmission. Such an analysis is only possible using TDS techniques, where a single bipolar pulse irradiates the sample. The time-domain analysis of this resonance also serves as a measure of the lifetime (and ultimately propagation distance) of the SPPs on the surface of the metal via either an exponential

fit to the decaying oscillation in the time domain, or the width of the resonance in the frequency domain.

Further work has analysed the effect of hole diameter on the lifetime of the SPP [79, 80]. Miyamaru [81] was the first to provide fits to the lifetimes of SPPs showing a decrease in lifetime as the diameter of the hole was increased. Neglecting ohmic losses, this decrease in lifetime was attributed to the increased scattering cross-section with increasing hole diameter, i.e. SPPs were scattered more frequently, as there was less distance between the holes. It is interesting to point out that similar effects observed in the optical regime (where the time domain cannot be directly accessed) are explained in terms of localised surface plasmons or shape effects [58, 78, 82].

A further complication regarding the variation of hole size is the magnitude of the coupling which is believed to exist between the SPPs and the non-resonant transmission. A detailed study by Han [83] measured the transmittance of rectangular apertures with varying hole widths. This study confirmed the results of previous work [71] in that the normalised peak transmission decreases with increasing hole width; however the results were found also to differ in that a redshift in peak frequency was observed with decreasing hole width, in line with results observed in the optical regime [43, 77, 78]. Further analysis revealed that the peak transmission initially increases, and then subsequently decreases, with increasing hole width. This suggests the existence of an optimal width; these results were interpreted using a Fano analysis. Typically, a Fano analysis provides a method to describe the coupling between a resonant and a non-resonant process, as is perceived to be the case for 2D hole arrays. Han argues that with increasing hole width, the degree of coupling to SPPs increases, whilst both the cut-off frequency and metal-filling fraction decreases; the latter two cases enabling a greater degree of non-resonant (direct) transmission. Furthermore, Han calculates that the coupling constant between the two regimes is found to increase with increasing hole width. Han concludes the analysis by stating that, as the hole width is increased, the combination of the increased direct transmission, the increased excitation of SPPs and the increased coupling between these two states leads to damping of the SPPs, broadening their resonance and shifting their peak to higher frequencies. This onset of the negative impact of the direct transmission through increasingly broader holes offers an explanation to the "optimum" hole width.

There exists only one experiment in which the length of the hole is varied, whilst the hole width and 2D period remain constant [84]. With the long axis of the hole aligned perpendicularly to the polarisation of the $E$-field, as the length of the hole is increased a redshift of the resonant frequency is observed. The authors attribute this shift to changing resonance regimes; for short hole lengths standard SPP modes are thought to dominate, whilst localised SPPs govern the transmission for longer hole lengths. This classification was supported by analysing the same arrays with two differing beam diameters. The arrays with the longest holes, where localised SPPs are thought to dominate, displayed very little change in transmission between the two beam diameters. A much greater dependence was observed for the shorter holes, where a vast difference in transmission was observed due to the effective collecting area of the array being reduced with the smaller beam diameter.

Further confirmation of this theory was presented by observing the change in peak transmission frequency when paper was placed next to the array. The theoretical work of Bravo-Abad [85] suggests holes of larger dimensions have a greater proportion of the $E$-field within the holes, whilst smaller holes have a greater proportion residing on the metal surface. This suggests larger holes should be less sensitive to a change in the neighbouring dielectric for two reasons: first, any established SPP is less dependent on the surface of the metal as a smaller proportion resides there; whilst, second, if the observed resonance is truly a localised SPP and only depends on the specific geometry of a single hole, it should be almost independent of the metal surface. This was observed to be the case as the paper was introduced: the smaller holes demonstrated a clear redshift in frequency, whilst the larger holes exhibited no shift.

Miyamaru [86] investigated the finite size effect for the transmission of hole arrays finding that, with more than 20 holes, a good quality band pass filter is achieved; and that ten holes were enough to observe EOT. The work of Matsui [87] investigated the transmission properties of random and aperiodic arrays. Random arrays found only to produce broad resonances which redshifted to lower frequencies when hole diameters were increased, suggesting waveguide cut-off was the dominant transmission factor. This ruled out the existence of so called "shape resonances" thought to exist for individual apertures. Aperiodic arrays (with 5, 12, and 18° rotational symmetry) were found to produce strong, sharp resonant features with a characteristic "Fano" asymmetrical appearance. Finally, note Qu [88] who observed so-called "fractal" surface plasmons. An abundance of resonances in the frequency domain was attributed to the interference between SPPs propagating in all directions of the metal hole array. This work not only highlights the long propagation distances involved with SPPs at THz frequencies, but also the unrestricted propagation directions of these excitations.

In conclusion: even with the considerable research activity, summarised above, into the THz transmission properties of metal hole arrays, no single theory has been found allowing resonances to be either explained or predicted. THz-TDS provides an elegant method to study the lifetime and properties of SPPs, including how they are strongly affected by hole and lattice geometries. The Fano interaction goes someway to matching the asymmetry of the resonances yet offers no real explanation as to the mechanisms involved or of the nature of the coupling interaction. Any theory seeking to explain the EOT anomaly must be able to explain, amongst other factors: the observed blueshift and broadening of a resonance with increasing hole width parallel to the polarisation; the redshift and broadening observed as hole length perpendicular to the polarisation is increased; the change in frequency associated with a change in period; and the reason that random arrays of holes produce no resonance.

## 21.3 Applications

### *21.3.1 Guiding THz Waves with Plasmons*

TDS systems, detailed elsewhere in this Volume, have been the "workhorse" for THz spectroscopy and imaging instrumentation for over a decade. Fibre-fed emitters and receivers have enabled the TDS systems to become more compact and flexible [89]. However, there still exists a requirement to eliminate the need for bulky parabolic mirror arrangements which are used to focus free space THz radiation onto a sample. Waveguides for SPPs provide a potential route to eliminate free-space THz optics in these systems. They enable THz radiation to be used to interrogate subwavelength samples for microscopy applications. In Sect. 21.2.4, we introduced the single wire waveguide; this has attracted much attention because of its design simplicity [90]. In its favour, the wire offers broadband guidance with low dispersion over long propagation distances [49]. However, it should be noted that, in practice, THz radiation is usually generated from dipole-based photoconductive emitters which produce a linearly polarised beam. The Sommerfeld wave on a wire is radially polarised; hence coupling from typical THz sources is inefficient [91]. Radially symmetric photoconductive antennas [51] have been developed which can overcome this problem. Alternatively, a diffraction/scattering type launch has been demonstrated on a patterned wire [92]. Grooves (500 $\mu$m wide, 100 $\mu$m deep with 1 mm period) circumferentially milled into a 1 mm stainless steel wire were shown to launch SPPs from an incident THz pulse. This approach enhances coupling from free-space THz radiation to the wire-guided SPPs; but leads to narrowing of the broadband pulse due to the inherent periodicity of the grooves.

Structuring of the wire itself is not essential, however, to achieve this result. Agrawal [93] showed that a bullseye arrangement could be used to couple SPPs onto a bare wire. Here, the wire was inserted into the centre of the aperture, so as to form a coaxial waveguide. The authors suggest that a TEM mode can be excited in this configuration, even with a linearly polarised source.

It should be noted that single wire-guided propagation has proved far less attractive in the microwave region, where a 10 mm diameter wire carries 75 % of its transmitted power at 10 GHz in a circular area of 400 mm radius around the wire [94]. However, at 1 THz, with a 100 $\mu$m wire, this radius is less that 1 mm [95]. Dielectric coatings can be used to confine the field but lead to dispersion [96]. As discussed previously, spoof SPPs provide an alternative route to further confine this radius [54]. To date, this has not been experimentally demonstrated at THz frequencies.

The deep subwavelength electric field confinement achievable by tapering the end of a wire has been exploited by Awad [97] for near-field imaging. Awad achieved a feature size resolution of $\lambda/50$ at a 0.3 THz centre frequency when imaging metal tracks on a GaAs substrate. Walther [98] developed a THz-TDS system without far-infrared parabolic optics. In this work, a 110 mm long, 254 $\mu$m diameter platinum/iridium wire with a sharp tip was placed in contact with a photoconductive emitter. Lactose powder, dispersed along 55 mm of the wire, showed characteristic

absorption at 0.53 THz. Interestingly, the wire-guided approach was found to be less susceptible to water vapour in the atmosphere than is the case for free-space THz TDS, thus avoiding the need for nitrogen purging during scanning. This is an important practical step towards field-deployable systems, where nitrogen purging is undesirable.

An alternative to wire-guiding is to use planar plasmonic devices. It is interesting in this regard to note that Ulrich and Tacke [99] first suggested that periodic metal structures, based on simple wire meshes, may be valuable as THz waveguides. Devices commonly available at microwave frequencies such as straight waveguides, $Y$-splitters and 3dB-couplers have been fabricated for THz applications from arrays of periodically perforated metal films [100]. These operate in the spoof SPP regime and show tight confinement and low propagation loss.

### 21.3.2 Manipulation: Modulators and Switches

THz modulators and switches are essential components of THz circuits, for use in such diverse areas as on-chip sensing, broad-band communication [101] and imaging. For example, if fast THz modulators could be further developed, they could replace mechanical scanners and speed up imaging, as has been demonstrated recently [102] with a single-pixel THz imaging system that includes a spatial modulator as a crucial component. Another significant application will be the development of phased-array radar that incorporate phase modulators that can be used to direct THz beams. Plasmonic technologies have great promise in delivering modulators and switches that are fast, have good depth of modulation, require low power levels for implementation and can be satisfactorily operated at room temperature. Furthermore, plasmon-based modulators, which are realised using micromachining technology, can be produced on the same semiconductor chip as plasmon-interconnect (see previous section), which offers considerable design flexibility.

Manipulation devices of this type rely on external perturbations to change their THz optical transmission or reflection. Such perturbations might include: magnetic and electric fields, optical probes or temperature changes. In practice, electrically addressable modulators are likely to be of most practical use in the future development of THz systems. Recently, metamaterial devices, that incorporate repeated numbers of elements such as split-ring resonators on a subwavelength scale, have been reported [103–106]. Since metamaterial devices are beyond the scope of this chapter, their performance will not be reviewed here, although it should be noted that SPP effects are essential to their operation.

Pan [107] demonstrated the use of a magnetically controlled nematic liquid crystal (NMC) to vary the transmission properties of a 2D metallic hole array. The NMC occupies the holes in the array and, as the refractive index is changed, so does the effective permeability of the device leading, in turn, to a shift in the SPP absorption frequency and transmission. Although this is far too slow to be utilised practically, it is noteworthy that the idea of changing the refractive index of a material placed in

the orifices of the array has been deployed to create an optically addressable device operating on the ps timescale [108]. As an alternative to modifying the refractive index of the liquid "filler" through its photophysical properties, Gómez Rivas [109] reported the use of an optical perturbation of the SPP characteristics through changes in the carrier density of a semiconductor (indium antimonide) slab interfaced to air. The authors claim modulation of the in-plane THz transmission is possible with ultra-low optical (532 nm) fluences and with a picosecond response time. In a more direct arrangement, Hendry [110] describes how the THz frequency transmission properties of a single slit through a silicon slab, decorated with surface corrugations on both faces, may be controlled optically so as to produce an enhancement of transmission with a very short response time.

Thermal perturbations of the electrical properties of a semiconductor, along the surface of which THz frequency SPPs are propagating, are likely to be far too slow to be of practical relevance. Nevertheless, it may be noted that an experimental investigation of this effect, for indium antimonide surfaces, is reported by Gómez Rivas [111] and a theoretical analysis is provided by Sanchez-Gil [112].

Nishimura [113] argued that metamaterials-based modulator devices may not have the necessary required performance characteristics as a result of conduction and radiation losses in conventional materials. These authors have proposed to harness 2D plasmon effects associated with the channel of a high electron mobility transistor (HEMT). This follows the work of Dyakonov and Shur [114], who noted that 2D plasmons could travel at a greater rate along the HEMT channel than is permitted for individual carriers. Nishimura et al. have modelled a gated HEMT structure operating as a THz transmission modulator and found that a 60 % extinction ratio and very fast operation at frequencies of up to 10 THz is possible.

### 21.3.3 Engineering the THz Wavefront with Plasmonic Devices

Lezec [115] first pointed out the possibility that the directionality of light emerging from a small aperture might be controlled through the use of a bullseye structure surrounding the aperture. These authors argued that: as the light falling upon a small aperture surrounded by corrugations was coupled to SPPs at specific angles for a given wavelength; so the reverse process might occur for corrugations on the exit surface. Agrawal [42] demonstrated this effect for the first time at THz frequencies. Chen [116] designed tunable plasmonic lenses, based on indium antimonide microslits, but has reported experimental validation. The emergence of the THz Quantum Cascade Laser (QCL) as a practical, compact THz frequency source, that might potentially operate at room temperature [117], has led to further significant activity in the development of plasmonic devices formed on the output facet of a QCL. Yu [118] argued that suitably designed plasmonic structures on QCL facets could achieve enhanced performance or new functionality in the near- and far-fields, an area that was termed "wavefront engineering." Examples include lasers with: high colli-mation, polarisation control, super-focussing in the near- and far-fields, beam steering

from a single device and the formation of beams with specific angular momentum. Akalin [119] reviewed these claims for plasmonic beam shapers, comparing them with the performance of external silicon lenses and horn antennas which reduce the impedance mismatch at the laser facet. Recently, Yu [120] reported the first real implementation of the concept of wavefront engineering. With a simple 1D grating design, the beam divergence reduced from approximately 180° to 10° which resulted in significant increases in power collection efficiency in comparison with unpatterned devices. The structure was incorporated onto the substrate below the laser aperture, without compromising the high temperature performance of the device. In the case of this particular structure, Yu argues that THz radiation from the aperture is coupled into spoof SPPs, instead of being directly radiated into the far-field.

### 21.3.4 Sensing

Almost all of the THz plasmonic sensing applications reported to date harness the dependence of the SPP resonant frequency on the properties of the interfacing dielectric. Two-dimensional hole arrays provide an easy method to exploit such properties, where SPPs are readily excited and confined to distances within the order of a wavelength. The first example of this in the THz regime was reported in 2005 by Tanaka [121]. Here, thin polypropylene films of varying thickness were attached to a 2D aluminium hole array. As the thickness of the dielectric film was increased, the resonant frequency of the SPPs was found to redshift, whilst the power transmittance was found to rapidly decrease. If a dielectric film were placed on both sides of the array, power transmittance was found to decrease less severely due to efficient coupling of SPPs on either side of the array. Such effects were even observed for film thicknesses much thinner than the wavelength of radiation used.

The sensitivity of SPPs to very thin (extreme subwavelength) layers of dielectric was demonstrated by Miyamaru [80], where a clear shift in resonant frequency was observed between printed paper and clear paper. This work also reported the effects of increasing the amount of glycerine absorbed on a nylon membrane attached to the hole array. Redshifts could be observed for quantities as small as 800 pL, with an accuracy of $\pm 0.2$ THz quoted for the peak frequency. Miyamaru argues that the long "lifetime" of the SPPs enhances the absorption process of the THz radiation in the sample under investigation. Yoshida [122] was the first to demonstrate biological sensing, detecting femtomol quantities of horseradish peroxidase on a 2D hole array. This work highlights that the observed shift in resonance frequency is of paramount importance in detecting small amounts of proteins; it also demonstrates the increased sensitivity of the plasmonic method over conventional THz-TDS techniques.

Further work has been undertaken to investigate the effects of a dielectric layer of an asymmetric metal–dielectric interface. In this study, increasing thicknesses of photoresist were spin-coated onto a lithographically defined aluminium hole array on silicon [123]. Miyamaru [124] investigated the reflection properties of hole arrays when changing the neighbouring dielectric. Dramatic redshifts and transmission

enhancements were observed and ascribed to the increased field confinement around the apertures as a result of the presence of the dielectric layer. Yoshida [125] using free-standing arrays exploited the existence of a sharp dip observed in the standard resonance peak of the array. This feature made it easier to detect slight shifts in frequency, thus improving the sensitivity of the sensor. Finally, Tian [126] embedded 2D stainless steel hole arrays into a quartz sample cell. Different isotopes of liquid methanol were then introduced into the cell, where shifts in the SPP resonant frequency were observed as the sample was changed. The shifts in frequency allowed the isotopes to be distinguished more accurately than by standard THz-TDS. This work also highlighted how liquids can be used as the neighbouring dielectric, instead of the solid films used previously. Further theoretical work proposes SPP-like fibre based sensors for the detection of gaseous samples [127], where sensor resolutions of the order of $10^{-4}$ Refractive Index Units (RIU) are predicted.

The use of SPPs in the infrared region of the spectrum has been exploited for decades to monitor binding interactions. THz radiation is extremely sensitive to low frequency intermolecular environments; so it might be argued that THz-SPPs could offer an even more sensitive technique for the analysis of biological binding interactions than currently possible using infrared methods.

### 21.3.5 Imaging

THz imaging often suffers from poor resolution owing to the long wavelengths of the radiation involved. It has been suggested that extreme confinement of radiation on corrugated wires using SPPs may improve spatial resolution in THz images [54, 90]. There are, however, many practical problems (e.g. coupling efficiencies) that may preclude realisation of this concept. Nevertheless, there are considerable opportunities to exploit plasmonic phenomena in near-field imaging using apertures, which is a well-established method for THz near-field microscopy [128]. The applicability of the technique is limited by the low transmission through a subwavelength aperture. However, by surrounding an aperture with periodic corrugations whose period matches the frequency of operation of THz source, a dramatic enhancement of the signal through the aperture can be achieved leading to greater transmission and improved spatial resolution. This has been demonstrated by Ishihara et al., where 100 μm apertures were surrounded by periodic corrugations, and illuminated with a THz-wave parametric oscillator [129]. Large transmission enhancements were observed at wavelengths commensurate with the period of the corrugations. Resolution tests of the apertures showed that 50 μm (i.e. $\lambda/4$) resolution was achieved. Transmission artefacts were observed when periodic corrugations were situated at either side of the apertures and attributed to the decoupling of SPPs on the far side of the hole. Planarized arrays were found to yield no such artefacts; however, they did display a field enhancement when the resolution test-piece was brought close to the aperture. Further work by Ishihara et al. used the same periodic structures but replaced the circular aperture with a bow-tie shape [130]. The greater field confinement associated with this shape led to an increased resolution of $\lambda/17$. Besides these

two examples, plasmonic apertures have not yet been exploited for near-field THz imaging elsewhere. The ability to greatly enhance transmission and control output beam shape [120] whilst still beating the diffraction limit, may provide a strong impetus to THz near-field imaging.

A further demonstration of plasmon-assisted THz imaging has been reported using 2D hole arrays [131]. By fabricating hole arrays of different periodicities, imaging could be achieved at a range of frequencies by placing the arrays, in-turn, in contact with the desired object. Raster scanning of a focussed THz beam over the array allowed a plasmon-assisted image to be acquired. It was found the presence of the hole array allowed for the detection of a soluble ink pattern on paper, which could not be detected without the array. Such increased sensitivity was further displayed by imaging a fingerprint on a polypropylene film. The final example of plasmon-assisted THz imaging takes a completely different approach and requires no actual device to be fabricated. Maraghechi [132] shows that, by embedding a dielectric object inside a random array of subwavelength metallic particles, the successful coupling, re-radiation and near-field propagation of plasmons allow the object to be spatially resolved. The subwavelength size of the metallic particles results in the "metal" possessing a positive real permittivity, effectively becoming a dielectric at THz frequencies. The embedded object thus behaves as one dielectric embedded within an outer dielectric. This means that the whole experiment resembles traditional non-destructive THz imaging of dielectric objects. Reconstruction algorithms allow the raw data to be enhanced, providing a ninefold increase in spatial resolution. This approach could be valuable for biological imaging and sensing at THz frequencies: if subwavelength gold particles could be dispersed on, or in, a biological sample (thereby providing an SPP resonance of a known frequency) superior sensitivity would be achieved.

The few examples which do exist in the literature of plasmon assisted imaging at THz frequencies demonstrate the distinct advantages over standard imaging techniques. These include: increased field confinement at the tip of a wire; enhanced transmission through very small aperture sizes; and superior volume sensitivity via the use of a 2D hole array.

## 21.4 Conclusion

In this chapter, we have reviewed the essential physics and some of the early applications of surface plasmons and plasmonic devices. Almost certainly other applications will soon emerge in such new fields as quantum entanglement [133] and slow light [134] in addition to further developments in all of the areas considered above. The realisation of such essential active components as cheaper broadband THz systems [135] and THz QCLs that operate at, or close to, room temperature will encourage the design and development of plasmonic structures with new functionality, leading to significant advances in THz communications, microscopy, communications, sensing and imaging. The fact that plasmonic devices can easily be made using standard clean room techniques will provide an additional impetus to this field.

# References

1. E.C.L. Ru, P.G. Etchehoin, *Principles of Surface Enhanced Raman Spectroscopy and Related Plasmonic Effects* (Elsevier, Amsterdam, 2008)
2. M.F. Kimmitt, *Far Infrared Techniques* (Pion Ltd., London, 1970)
3. T. Dumelow, D.R. Tilley, J. Opt. Soc. Am. A **10**(4), 633–645 (1993)
4. E.D. Palik, J.K. Furdyna Rep, Prog. Phys. **33**(12), 1193 (1970)
5. D. Pines, *Elementary Excitations in Solids: Lectures on Protons, Electrons and Plasmons* (Perseus Press, Reading, MA, 1999)
6. J.B. Pendry, L. Martin-Moreno, F.J. Garcia-Vidal, Science **305**(5685), 847–848 (2004)
7. H. Raether, *Surface Plasmons on Smooth and Rough Surfaces and on Gratings* (Springer, Berlin, 1988)
8. S.A. Maier, *Plasmonics: Fundamentals and Applications* (Springer, New York, 2007)
9. F. Medina, F. Mesa, R. Marques, IEEE T. Microw. Theory **56**(12), 3108–3120 (2008)
10. T.W. Ebbesen, H.J. Lezec, H.F. Ghaemi, T. Thio, P.A. Wolff, Nature **391**(6668), 667–669 (1998)
11. J.G. Rivas, C. Schotsch, P. H. Bolivar, H. Kurz Phys. Rev. B **68**(20), 201306 (2003)
12. F.J. Garcia-Vidal, L. Martin-Moreno, T.W. Ebbesen, L. Kuipers Rev, Mod. Phys. **82**(1), 729–787 (2010)
13. F.J.G. de Abajo Rev, Mod. Phys. **79**(4), 1267–1290 (2007)
14. H.A. Bethe Phys, Rev. **182**(7–8), 163–182 (1944)
15. M.C. Hutley, V.M. Bird Opt, Acta **20**(10), 771–782 (1973)
16. Y.Y. Teng, E.A. Stern Phys, Rev. Lett. **19**(9), 511 (1967)
17. W. Withayachumnankul, D. Abbott, IEEE Photon. J. **1**(2), 99–118 (2009)
18. A.P. Hibbins, B.R. Evans, J. R. Sambles Science **308**(5722), 670–672 (2005)
19. A.P. Hibbins, M.J. Lockyear, J.R. Sambles, Phys. Rev. B **76**, 16 (2007)
20. G. Acuna, S.F. Heucke, F. Kuchler, H.T. Chen, A.J. Taylor, R. Kersting Opt, Express **16**(23), 18745–18751 (2008)
21. M. Navarro-Cia, M. Beruete, S. Agrafiotis, F. Falcone, M. Sorolla, S.A. Maier Opt, Express **17**(20), 18184–18195 (2009)
22. J.R. Sambles, G.W. Bradbery, F.Z. Yang Contemp, Phys. **32**(3), 173–183 (1991)
23. A. Sihvola, J.R. Qi, I. V. Lindell IEEE Antennas Propag. **52**(1), 124–136 (2010)
24. J. Zenneck Ann, Phys. **23**(10), 846–866 (1907)
25. M.A. Ordal, L.L. Long, R.J. Bell, S.E. Bell, R.R. Bell, R.W. Alexander, C.A. Ward Appl, Opt. **22**(7), 1099–1119 (1983)
26. J.G. Rivas, A. Berrier, Asia Pac. Microwave Conf. **1–5**, 1293–1296 (2009)
27. J. Homola Anal, Bioanal. Chem. **377**(3), 528–539 (2003)
28. H. Hirori, K. Yamashita, M. Nagai, K. Tanaka Jpn, J. Appl. Phys. **2**(43), L1287–L1289 (2004)
29. J.F. O'Hara, R.D. Averitt, A.J. Taylor Opt, Express **13**, 6117–6126 (2005)
30. E.V. Alieva, Y.E. Petrov, V.A. Yakovlev, E.R. Eliel, E.W.M. van der Ham, Q.H.F. Vrehen, A.F.G. van der Meer, V. A. Sychugov. JETP Lett. **66**(9), 609–613 (1997)
31. J.G. Rivas, M. Kuttge, P.H. Bolivar, H. Kurz, J.A. Sanchez-Gil Phys, Rev. Lett. **93**(25), 256804 (2004)
32. T.H. Isaac, J.G. Rivas, J.R. Sambles, W.L. Barnes, E. Hendry Phys, Rev. B **77**(11), 113411 (2008)
33. I.P. Kaminow, W.L. Mammel, H.P. Weber Appl, Opt. **13**(2), 396–405 (1974)
34. J. Saxler, J.G. Rivas, C. Janke, H.P.M. Pellemans, P.H. Bolivar, H. Kurz Phys, Rev. B **69**(15), 155427 (2004)
35. T.H. Isaac, W.L. Barnes, E. Hendry Appl, Phys. Lett. **93**(24), 241115 (2008)
36. T.I. Jeon, D. Grischkowsky Appl, Phys. Lett. **85**(25), 6092–6094 (2004)
37. M.F. Gong, T.I. Jeon, D. Grischkowsky Opt, Express **17**(19), 17088–17101 (2009)
38. W.Q. Zhu, A. Nahata Opt, Express **15**(9), 5616–5624 (2007)

39. K.G. Lee, H.W. Kihm, J.E. Kihm, W.J. Choi, H. Kim, C. Ropers, D.J. Park, Y.C. Yoon, S.B. Choi, H. Woo, J. Kim, B. Lee, Q.H. Park, C. Lienau, D. S. Kim Nature Photon. **1**, 53–56 (2007)
40. H. Caglayan, I. Bulu, E. Ozbay Opt, Express **13**(5), 1666–1671 (2005)
41. A. Agrawal, H. Cao, A. Nahata. New J. Phys. **7**, 249 (2005)
42. A. Agrawal, H. Cao, A. Nahata Opt, Express **13**, 3535–3542 (2005)
43. H. Cao, A. Agrawal, A. Nahata Opt, Express **13**, 763–769 (2005)
44. A. Agrawal, A. Nahata, Opt. Express **14**, 1973–1981 (2006)
45. G. Goubau, J. Appl. Phys. **21**(11), 1119–1128 (1950)
46. C.R. Williams, S.R. Andrews, S.A. Maier, A.I. Fernandez-Dominguez, L. Martin-Moreno, F. J. Garcia-Vidal Nature Photon. **2**(3), 175–179 (2008)
47. A.P. Hibbins, E. Hendry, M.J. Lockyear, J.R. Sambles Opt, Express **16**(25), 20441–20447 (2008)
48. E. Sommerfeld, Ann. Phys. Chem **67**, 233–290 (1899)
49. K. L. Wang, D.M. Mittleman, Nature **432**(7015), 376–379 (2004)
50. Y.B. Ji, E.S. Lee, J.S. Jang, T.I. Jeon Opt, Express **16**(1), 271–278 (2008)
51. T.I. Jeon, J.Q. Zhang, D. Grischkowsky Appl, Phys. Lett. **86**(16), 031104 (2005)
52. V. Astley, H. Zhan, R. Mendis, D.M. Mittleman, in *Conference on Lasers and Electro-Optics and Quantum Electronics and Laser Science* (New York, USA, 2009), pp. 1720–1721
53. V. Astley, J. Scheiman, R. Mendis, D.M. Mittleman Opt, Lett. **35**(4), 553–555 (2010)
54. S.A. Maier, S.R. Andrews, L. Martin-Moreno, F.J. Garcia-Vidal Phys, Rev. Lett. **97**(17), 176805 (2006)
55. K.J. Chau, A.Y. Elezzabi Phys, Rev. B **72**(7), 075110 (2005)
56. W.L. Barnes, W.A. Murray, J. Dintinger, E. Devaux, T.W. Ebbesen Phys, Rev. Lett. **92**(10), 107401 (2004)
57. S.A. Darmanyan, A.V. Zayats, Phys. Rev. B **67**(3), 035424 (2003)
58. A. Degiron, T.W. Ebbesen, J Opt. A. - Pure Appl. Op. **7**, S90–S96 (2005)
59. Z.Y. Fan, L. Zhan, X. Hu, Y.X. Xia Opt, Commun. **281**(21), 5467–5471 (2008)
60. H.F. Ghaemi, T. Thio, D.E. Grupp, T.W. Ebbesen, H.J. Lezec Phys, Rev. B **58**(11), 6779–6782 (1998)
61. A. Krishnan, T. Thio, T.J. Kima, H.J. Lezec, T.W. Ebbesen, P.A. Wolff, J. Pendry, L. Martin-Moreno, F.J. Garcia-Vidal Opt, Commun. **200**(1–6), 1–7 (2001)
62. L. Martin-Moreno, F.J. Garcia-Vidal, H.J. Lezec, K.M. Pellerin, T. Thio, J.B. Pendry, T.W. Ebbesen Phys, Rev. Lett. **86**(6), 1114–1117 (2001)
63. A. Mary, S.G. Rodrigo, L. Martin-Moreno, F.J. Garcia-Vidal Phys, Rev. B **76**(19), 159414 (2007)
64. Z.C. Ruan, M. Qiu Phys, Rev. Lett. **96**(23), 233901 (2006)
65. U. Schroter, D. Heitmann Phys, Rev. B **58**(23), 15419–15421 (1998)
66. M.M.J. Treacy Phys, Rev. B **66**(19), 195105 (2002)
67. J.M. Vigoureux Opt, Commun. **198**(4–6), 257–263 (2001)
68. S.M. Williams, J.V., Coe Plasmonics **1**, 87–93 (2006)
69. J.V. Coe, J.M. Heer, S. Teeters-Kennedy, H. Tian, K.R. Rodriguez Annu, Rev. Phys. Chem. **59**, 179–202 (2008)
70. D.X. Qu, D. Grischkowsky, W.L. Zhang Opt, Lett. **29**(8), 896–898 (2004)
71. H. Cao, A. Nahata Opt, Express **12**(16), 3664–3672 (2004)
72. A.K. Azad, Y.G. Zhao, W.L. Zhang, M.X. He Opt, Lett. **31**(17), 2637–2639 (2006)
73. A.K. Azad, W.L. Zhang Opt, Lett. **30**(21), 2945–2947 (2005)
74. Z. Tian, R. Singh, J.G. Han, J.Q. Gu, Q.R. Xing, J. Wu, W.L. Zhang Opt, Lett. **35**(21), 3586–3588 (2010)
75. C. Janke, J.G. Rivas, C. Schotsch, L. Beckmann, P.H. Bolivar, H. Kurz Phys, Rev. B **69**(20), 205314 (2004)
76. A.K. Azad, Y. Zhao, W. Zhang Appl, Phys. Lett. **86**(14), 141102 (2005)
77. A. Degiron, H.J. Lezec, N. Yamamoto, T.W. Ebbesen Opt, Commun. **239**(1–3), 61–66 (2004)

78.  K.J.K. Koerkamp, S. Enoch, F.B. Segerink, N.F. van Hulst, L. Kuipers Phys, Rev. Lett. **92**(18), 183901 (2004)
79.  T.H. Isaac, W.L. Barnes, E. Hendry Phys, Rev. B **80**(11), 115423 (2009)
80.  F. Miyamaru, M. Tanaka, M. Hangyo Phys, Rev. B **74**(15), 153416 (2006)
81.  F. Miyamaru, S. Hayashi, C. Otani, K. Kawase, Y. Ogawa, H. Yoshida, E. Kato Opt, Lett. **31**(8), 1118–1120 (2006)
82.  K.L. van der Molen, K.J.K. Koerkamp, S. Enoch, F.B. Segerink, N.F. van Hulst, L. Kuipers Phys, Rev. B **72**(4), 045421 (2005)
83.  J.G. Han, A.K. Azad, M.F. Gong, X.C. Lu, W.L. Zhang Appl, Phys. Lett. **91**(7), 071122 (2007)
84.  F. Miyamaru, M.W. Takeda Phys, Rev. B **79**(15), 153405 (2009)
85.  J. Bravo-Abad, L. Martin-Moreno, F.J. Garcia-Vidal, E. Hendry, J.G. Rivas, Phys. Rev. B **76**(24), 241102(R) (2007)
86.  F. Miyamaru, M. Hangyo Appl, Phys. Lett. **84**(15), 2742–2744 (2004)
87.  T. Matsui, A. Agrawal, A. Nahata, Z. V. Vardeny. Nature **446**(7135), 517–521 (2007)
88.  D.X. Qu, D. Grischkowsky Phys, Rev. Lett. **93**(19), 196804 (2004)
89.  http://www.Teraview.Com/terahertz/id/74, Teraview, Accessed 22 December 2010
90.  V. Astley, R. Mendis, D.M. Mittleman Appl, Phys. Lett. **95**(3), 031104 (2009)
91.  J.A. Deibel, K. Wang, M. Escarra, N. Berndsen, D.M. Mittleman, C.R. Acad., Sci. II B **9**(2), 215–231 (2008)
92.  H. Cao, A. Nahata Opt, Express **13**(18), 7028–7034 (2005)
93.  A. Agrawal, A. Nahata Opt, Express **15**(14), 9022–9028 (2007)
94.  M. J. King, J. C. Wiltse, IEEE T. Antenn. Propag. **10**(3), 246–254 (1962)
95.  M. Wachter, M. Nagel, H. Kurz Opt, Express **13**, 10815–10822 (2005)
96.  N.C.J. van der Valk, P.C.M. Planken Appl, Phys. Lett. **87**(7), 071106 (2005)
97.  M. Awad, M. Nagel, H. Kurz Appl, Phys. Lett. **94**(5), 051107 (2009)
98.  M. Walther, M.R. Freeman, F.A. Hegmann Appl, Phys. Lett. **87**(26), 261107 (2005)
99.  R. Ulrich, M. Tacke Appl, Phys. Lett. **22**(5), 251–253 (1973)
100. W.Q. Zhu, A. Agrawal, A. Nahata Opt, Express **16**(9), 6216–6226 (2008)
101. T. Kleine-Ostmann, K. Pierz, G. Hein, P. Dawson, M. Koch Elec, Lett. **40**(2), 124–126 (2004)
102. W.L. Chan, K. Charan, D. Takhar, K.F. Kelly, R.G. Baraniuk, D.M. Mittleman Appl, Phys. Lett. **93**(12), 121105 (2008)
103. W.L. Chan, H.T. Chen, A.J. Taylor, I. Brener, M.J. Cich, D.M. Mittleman Appl, Phys. Lett. **94**(21), 213511 (2009)
104. H.T. Chen, S. Palit, T. Tyler, C.M. Bingham, J.M.O. Zide, J.F. O'Hara, D.R. Smith, A.C. Gossard, R.D. Averitt, W.J. Padilla, N.M. Jokerst, A.J. Taylor Appl, Phys. Lett. **93**(9), 091117 (2008)
105. M. Jarrahi, IEEE Phot. Soc. Winter Topicals Meeting Series **57**, 56–57 (2010)
106. S. Zarei, M. Jarrahi, IEEE Phot. Soc. Winter Topicals Meeting Series 30–31 (2010)
107. C.L. Pan, C.F. Hsieh, R.P. Pan, M. Tanaka, F. Miyamaru, M. Tani, M. Hangyo Opt, Express **13**(11), 3921–3930 (2005)
108. J. Dintinger, I. Robel, P.V. Kamat, C. Genet, T.W. Ebbesen Adv, Mater. **18**(13), 1645–1648 (2006)
109. J.G. Rivas, J.A. Sanchez-Gil, M. Kuttge, P.H. Bolivar, H. Kurz Phys, Rev. B **74**, 245324 (2006)
110. E. Hendry, F.J. Garcia-Vidal, L. Martin-Moreno, J.G. Rivas, M. Bonn, A.P. Hibbins, M.J. Lockyear Phys, Rev. Lett. **100**(12), 123901 (2008)
111. J.G. Rivas, M. Kuttge, H. Kurz, P.H. Bolivar, J.A. Sanchez-Gil Appl, Phys. Lett. **88**(8), 082106 (2006)
112. J.A. Sanchez-Gil, J.G. Rivas Phys, Rev. B **73**, 205410 (2006)
113. T. Nishimura, N. Magome, T. Otsuji Jpn, J. Appl. Phys. **49**(5), 054301 (2010)
114. M. Dyakonov, M. Shur Phys, Rev. Lett. **71**(15), 2465–2468 (1993)
115. H.J. Lezec, A. Degiron, E. Devaux, R.A. Linke, L. Martin-Moreno, F.J. Garcia-Vidal, T. W. Ebbesen. Science **297**(5582), 820–822 (2002)

116. M.K. Chen, Y.C. Chang, C.E. Yang, Y.H. Guo, J. Mazurowski, S. Yin, P. Ruffin, C. Brantley, E. Edwards, C. Luo Opt, Techn. Let. **52**(4), 979–981 (2010)
117. G. Scalari, C. Walther, M. Fischer, R. Terazzi, H. Beere, D. Ritchie, J. Faist Laser & Photon. Rev. **3**(1–2), 45–66 (2009)
118. N.F. Yu, R. Blanchard, J.A. Fan, Q.J. Wang, M. Kats, F. Capasso, INEC: 2010 3rd Int. Nanoelectronics Conf. **1–2**, 70–71 (2010)
119. T. Akalin, W. Maineult, P. Gellie, E. Peytavit, A. Andronico, P. Filloux, G. Leo, J.F. Lampin, C. Sirtori, H.E. Beere, D.A. Ritchie, S. Barbieri, APMC: 2009 Asia Pac. Microwave Conf. **1–5**, 183–185 (2009)
120. N.F. Yu, Q.J. Wang, M.A. Kats, J.A. Fan, S.P. Khanna, L.H. Li, A.G. Davies, E.H. Linfield, F. Capasso Nature Mater. **9**(9), 730–735 (2010)
121. M. Tanaka, F. Miyamaru, M. Hangyo, T. Tanaka, M. Akazawa, E. Sano Opt, Lett. **30**(10), 1210–1212 (2005)
122. H. Yoshida, Y. Ogawa, Y. Kawai, S. Hayashi, A. Hayashi, C. Otani, E. Kato, F. Miyamaru, K. Kawase Appl, Phys. Lett. **91**(25), 253901 (2007)
123. J.G. Han, X.C. Lu, W.L. Zhang, J. Appl. Phys. **103**(3), 033108 (2008)
124. F. Miyamaru, Y. Sasagawa, M.W. Takeda Appl, Phys. Lett. **96**(2), 021106 (2010)
125. S. Yoshida, K. Suizu, E. Kato, Y. Nakagomi, Y. Ogawa, K. Kawase, J. Mol. Spectrosc. **256**(1), 146–151 (2009)
126. Z. Tian, J.G. Han, X.C. Lu, J.Q. Gu, Q.R. Xing, W.L. Zhang Chem, Phys. Lett. **475**(1–3), 132–134 (2009)
127. A. Hassani, M. Skorobogatiy Opt, Express **16**(25), 20206–20214 (2008)
128. R. Degl'Innocenti, M. Montinaro, J. Xu, V. Piazza, P. Pingue, A. Tredicucci, F. Beltram, H.E. Beere, D.A. Ritchie Opt, Express **17**(26), 23785–23792 (2009)
129. K. Ishihara, T. Ikari, H. Minamide, J. Shikata, K. Ohashi, H. Yokoyama, H. Ito Jpn, J. Appl. Phys. **2**(44), L929–L931 (2005)
130. K. Ishihara, K. Ohashi, T. Ikari, H. Minamide, H. Yokoyama, J. Shikata, H. Ito Appl, Phys. Lett. **89**(20), 201120 (2006)
131. F. Miyamaru, M.W. Takeda, T. Suzuki, C. Otani Opt, Express **15**, 14804–14809 (2007)
132. P. Maraghechi, C. Straatsma, Z. Liu, V. Zhao, A.Y. Elezzabi Opt, Express **17**(19), 16456–16464 (2009)
133. E. Altewischer, M.P. van Exter, J. P. Woerdman Nature **418**(6895), 304–306 (2002)
134. Q. Gan, Z. Fu, Y.J. Ding, F.J. Bartoli Phys, Rev. Lett. **100**(25), 256803 (2008)
135. C.C. Renaud, M. Pantouvaki, S. Gregoire, I. Lealman, P. Cannard, S. Cole, R Moore, R. Gwilliam, A.J. Seeds, IEEE J. Quantum Elect. **43**(11–12), 998–1005 (2007)